Open Ceramics 26 (2026) 100969

Contents lists available at ScienceDirect

Open Ceramics

journal homepage: www.sciencedirect.com/journal/open-ceramics

An innovative 3D printing approach for processing Si/SiOC anodes for Li-ion batteries with potential application as high areal energy and power density electrodes

Adane Muche Abebe [a,*], Rajat Chaudhary [a,b,*], Alexander Kempf [c], Sereno Sacchet [d], Luca Fambri [d], Mattia Biesuz [a], Magdalena Graczyk-Zajac [c,e], Gian Domenico Sorarù [a]

[a] Glass & Ceramics Lab, Department of Industrial Engineering, University of Trento, Via Sommarive 9, Povo 38123, Trento, Italy
[b] Consorzio Interuniversitario Nazionale per la Scienza e Tecnologia dei Materiali, Via Giuseppe Giusti, 9, 50121 Firenze, Italy
[c] Institute of Materials Science, Technical University of Darmstadt, Otto-Berndt-Str. 3, Darmstadt 64287, Germany
[d] Polymer & Composite Lab, Department of Industrial Engineering, University of Trento, Via Sommarive 9, Povo 38123, Trento, Italy
[e] EnBW Energie Baden-Württemberg AG, Durlacher Allee 93, Karlsruhe 76131, Germany

ARTICLE INFO

Keywords:
SiNPs/SiOC composite
Polymer-derived ceramics
Lithium-ion battery

ABSTRACT

A facile method for fabricating a silicon nanoparticle–silicon oxycarbide composite anode material for lithium-ion batteries is developed using the polymer-derived ceramic (PDC) route. A cellular structure has first been printed via fused filament fabrication (FFF) using a Si nanoparticle-loaded thermoplastic polyurethane (TPU) filament, and subsequently infiltrated with a preceramic polymer, crosslinked at 160 °C, and pyrolyzed at 900 °C under nitrogen. For comparison, a pure SiOC ceramic has also been fabricated under identical conditions using commercial TPU filament. X-ray diffraction confirms the dispersion of Si nanoparticles within an amorphous SiOC matrix, while thermogravimetric analysis reveals free carbon contents of 39 wt% (SiOC) and 24 wt% (SiNPs/SiOC). Incorporation of Si nanoparticles into the SiOC matrix leads to improved reversible capacity, cyclic stability, and rate capability. The SiNPs/SiOC composite delivers initial reversible capacities of 990, 800, and 740 mAh g^{-1} at current densities of C/20, C/10, and C/5, respectively.

1. Introduction

Li-Ion batteries, LIB, are widely used as an energy device for all kinds of portable electronics. Their relevance is quickly expanding with the electrification of the automotive industry, with a volume growth of about x10 in the last 5 years [1] There is still a need for devices with higher energy and power density, such as power sources for electrically driven cars or large-scale stationary energy storage. As a result, new high-capacity electrode materials need to be found. Graphite is the most widely used anode material in lithium-ion batteries (LIBs), owing to its high electrical conductivity, excellent rechargeability, and low volume expansion [2]. However, graphite possesses a relatively low theoretical capacity (372 mAh g^{-1}) and poses safety concerns at high charging rates [3,4]. The most studied anode materials to replace graphite are Si and Sn [5] Silicon, in particular, is a promising contender due to its exceptionally high theoretical capacity of 3600 mAh g^{-1}, but large volume changes during lithiation and delithiation limit its uses [6] Sn presents a similar drawback with the theoretical lithiation capacity of 994 mAh g^{-1} [7]

Recently, various Si-based polymer-derived ceramics (PDCs), such as SiCN and SiOC, have been investigated as potential substitutes for graphite in LIBs due to their excellent electrochemical properties, including high reversible capacities of up to 1300 mAh g^{-1} [4,8–18] In particular, carbon-rich SiOC ceramics, having an amorphous structure, which include mixed silicon oxycarbide units, clusters of free carbon, and microporosity, demonstrate excellent Li storage in comparison to graphite [19,20]. Building on these achievements, many researchers have explored the synergistic combination of Si and SiOC to develop new anode materials with enhanced lithium storage capacity [21–26]. Moreover, the use of silicon oxycarbide ceramics as a host matrix for Si nanoparticles is especially promising: the low elastic modulus of the high C_{free} oxycarbide network [27] effectively buffers the volume expansion of Si particles during lithiation, preventing the buildup of high stresses and ultimately reducing capacity fading.

* Corresponding authors.
E-mail addresses: adanemuche.abebe@unitn.it (A.M. Abebe), rajat.chaudhary@unitn.it (R. Chaudhary).

https://doi.org/10.1016/j.oceram.2026.100969
Received 3 April 2026; Received in revised form 24 April 2026; Accepted 4 May 2026
Available online 5 May 2026

The present work contributes to this line of research by employing an innovative and straightforward 3D printing approach, [28] previously used to process SiC/SiOC composite materials and structures, [29] to obtain SiNPs/SiOC composites. Specifically, a silicon nanoparticle/thermoplastic polyurethane (SiNPs/TPU) filament was 3D-printed via fused filament fabrication (FFF) into a cellular structure, which was subsequently impregnated with a preceramic polymer (polysilazane) and pyrolyzed at 900 °C under a nitrogen flow. The resulting material is a cellular SiNPs/SiOC composite. In this study, although the material was obtained in the form of a cellular structure, it was ground into powder to evaluate the electrochemical performance of the material as an anode for lithium-ion storage. It is important to emphasize that the 3D printing approach offers significant potential for the fabrication of tailored anodic architectures with high areal energy and power densities [30,31]

2. Experimental

2.1. Synthesis of sinps/sioc

Thermoplastic polyurethane (TPU, Ninjaflex) filament and silicon nanoparticles (Si, 99.9 %, 100 nm) were purchased from NinjaTek (Lititz, PA, USA) and SkySpring Nanomaterials, Inc. (Houston, TX, USA), respectively. The polysilazane precursor Durazane® 1800 was obtained from Merck (Darmstadt, Germany).

Ninjaflex TPU and Si nanoparticles (SiNPs) were compounded at a 85/15 wt % ratio using a Thermo Haake Rheomix 600 mixer (Thermo Fisher Scientific, USA). The resulting compound was extruded into filaments with a final diameter of approximately 1.75 mm. Further details of the compounding and extrusion procedures are reported elsewhere [29].

The TPU/SiNP filament was used to fabricate cellular components ($15 \times 15 \times 5$ mm^3) via fused filament fabrication (FFF) using a 0.25 mm nozzle. The printed scaffolds were immersed in an acetone solution containing a Pt catalyst for 15 min to promote swelling and catalyst absorption. Subsequently, the samples were infiltrated with the preceramic polymer Durazane for 6 h, allowing fully infiltration of the scaffolds and interaction with the platinum catalyst. The infiltrated structures were then air-dried for 48 h.

Pyrolysis was performed in an alumina tube furnace under an inert N_2 atmosphere. The furnace was purged with nitrogen for 2 h prior to heating. A heating rate of 2 °C min^{-1} was applied up to 160 °C, followed by a 3-hour dwell to enhance crosslinking. The temperature was then increased at 0.5 °C min^{-1} to 800 °C to minimize deformation during polyurethane decomposition and ceramization. After reaching 800 °C, the heating rate was raised to 2 °C min^{-1} up to 900 °C, with a 1-hour hold, followed by natural cooling.

This optimized thermal profile, derived from previous work on SiOC ceramics with varying wall thicknesses for bio-applications [32], yielded cellular SiNPs/SiOC composite structures. An analogous procedure was conducted using pure Ninjaflex filament to produce TPU scaffolds, which were subsequently infiltrated with Durazane and pyrolyzed to obtain reference SiOC structures. Finally, both SiNPs/SiOC and SiOC cellular samples were milled into powders for electrochemical characterization.

A schematic representation of the process leading to the SiNPs/SiOC composite material is reported in Fig. 1.

2.2. Electrode preparation

The 3D-printed ceramic samples (SiNPs/SiOC and SiOC) were first ground and then further milled using a Retsch MM 400 mixer mill at a frequency of 30 s^{-1} for 1 h. The milled powder was sieved to particle sizes ≤40 μm using a vibratory sieve shaker (Retsch VS 1000).

Electrodes were prepared by mixing 85 wt % SiNPs/SiOC or SiOC powders as the active material, 10 wt % binder (a 1:1 wt ratio of carboxymethyl cellulose (CMC) and styrene–butadiene rubber (SBR)), and 5 wt % carbon black as a conductive additive in deionized water using an IKA T25 digital ULTRA-TURRAX mixer for 30 min. The resulting slurry was cast onto copper foil with a doctor blade set to a 120 μm gap. The coated electrodes were dried at 40 °C for 12 h under ambient conditions, after which 10 mm diameter electrode disks were punched from the sheet.

The active mass of each electrode was determined by subtracting the

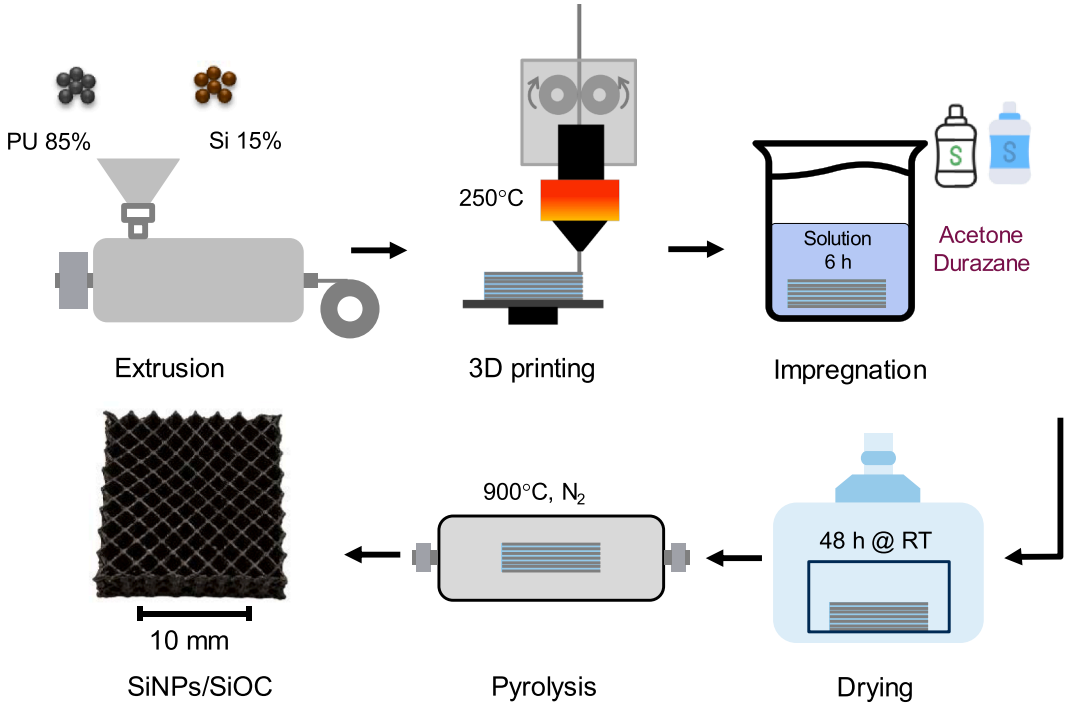

Fig. 1. Schematic representation of the synthesis of SiNPs/SiOC composite from SiNPs-PU filaments via polysilazane impregnation.

average mass of the blank Cu foil. The electrodes were then further dried in a Büchi glass oven (B-585) under vacuum at 80 °C for 24 h and directly transferred into an Ar-filled glovebox (O_2 and H_2O levels <0.1 ppm) for cell assembly.

Half-cells were assembled in a Swagelok-type configuration using lithium metal as the counter electrode (99.9 %, 0.75 mm thickness), quartz microfiber filters (QMA, Whatman) as the separator, and a custom electrolyte (VP1745) (see Fig. 2).

2.3. Structural characterization

The skeletal density (ρ_s) was measured using an Ultrapyc 5000 gas pycnometer (Anton Paar GmbH, Graz, Austria) at 20 °C with helium as the displacement gas.

Nitrogen physisorption isotherms for both samples were measured using a Quantachrome instrument (Anton Paar, USA) with nitrogen as the adsorbate at 77 K. Prior to analysis, the samples were degassed at 300 °C for 7 h to remove adsorbed species and ensure clean pore surfaces. The specific surface area was calculated using the BET (Brunauer, Emmett, and Teller) method, while the total pore volume and pore size distribution were determined using the BJH (Barrett-Joyner-Halenda) model.

Fourier transform infrared (FTIR) spectra were obtained in transmission mode with a Thermo Optics Avatar 330 spectrometer (Thermo Fisher Scientific, Waltham, MA, USA) using KBr pellets. Spectra were recorded in the 4000–400 cm^{-1} range with 64 scans at 4 cm^{-1} resolution.

X-ray diffraction (XRD) patterns were collected on powder samples using an IPD 3000 diffractometer (Italstructures, Italy) with a Cu anode (40 kV, 30 mA) and a multilayer monochromator (Goebel mirror). Data were acquired over a 2θ range of 10–120°, with a 0.02° step size and 1200 s acquisition time, using a Dectris Mythen 1 K hybrid pixel detector.

Scanning electron microscopy (SEM) imaging, along with elemental mapping of silicon (Si), carbon (C), and oxygen (O) for the SiNP/SiOC composite, was performed on fracture surfaces. The samples were mounted on conductive carbon tape and coated with a thin layer of Pt/Pd (80:20) via sputter deposition to minimize charging effects. The analyses were carried out using a SEM (JEOL JSM-IT300LV, Tokyo, Japan) operated at an accelerating voltage of 20 kV and equipped with an energy-dispersive X-ray spectroscopy (EDS) microprobe (Bruker XFlash 630 M detector, Germany).

2.4. Thermal analysis

Simultaneous thermal analysis (STA 449 F3 Jupiter, Netzsch-Geratebau GmbH, Selb, Germany) was conducted on SiOC and SiNPs/SiOC samples to investigate the oxidation of free carbon and silicon nanoparticles. Prior to the measurements, a blank run was performed under identical experimental conditions to create a correction curve and account for buoyancy effects. The analysis was carried out using approximately 25 mg of sample placed in an alumina crucible under purified air at a flow rate of 50 cm^3 min^{-1}. The samples were heated from 30 °C to 1450 °C at 10 °C min^{-1}, followed by a 2 h isotherm at 1450 °C to ensure complete oxidation. The TGA-DSC data were evaluated using Proteus software, while the FTIR spectra were synchronized with Bruker OPUS software, facilitating the identification of evolved gases from the integrated spectral libraries. The gases were continuously directed into a heated FTIR gas cell, maintained at 200 °C. Finally, all mass change, heat flow, and FTIR spectral data were recorded simultaneously as a function of time and temperature, enabling real-time identification of gaseous products over specified temperature ranges.

2.5. Electrochemical characterization

All electrochemical tests were performed on a Biologic Potentiostat instrument (VMP multipotentiostat, France) with an active mass loading of 2.0 - 3.5 mg cm^{-2}. Before each measurement, the system was stabilized under open-circuit conditions for 24 h. Galvanostatic charge-discharge cycling with potential limitation (GCPL) was conducted at 74.4 and 372 mA g^{-1}, in a potential window of 0.005 to 3.0 V. The rate capability tests were performed in the same voltage range using different C-rates, and the current was adjusted accordingly: 0.1C (3 cycles), 0.2C (5 cycles), 0.5C (10 cycles), 1C (10 cycles), 2C (10 cycles), 3C (10 cycles), and then back to 0.1C (3 cycles). Cyclic voltammetry (CV) measurements were carried out at a scan rate of 50 μV s^{-1} within the same potential range.

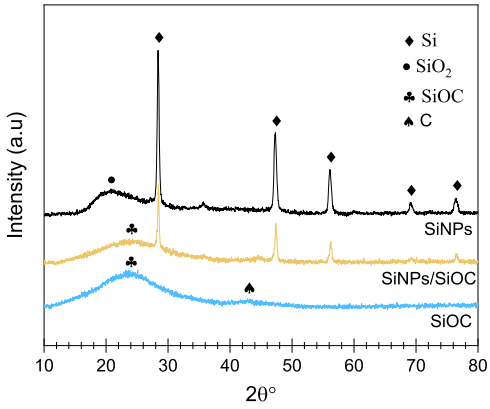

Fig. 3. XRD pattern of the SiNPs, SiOC ceramic and SiNPs/SiOC composite.

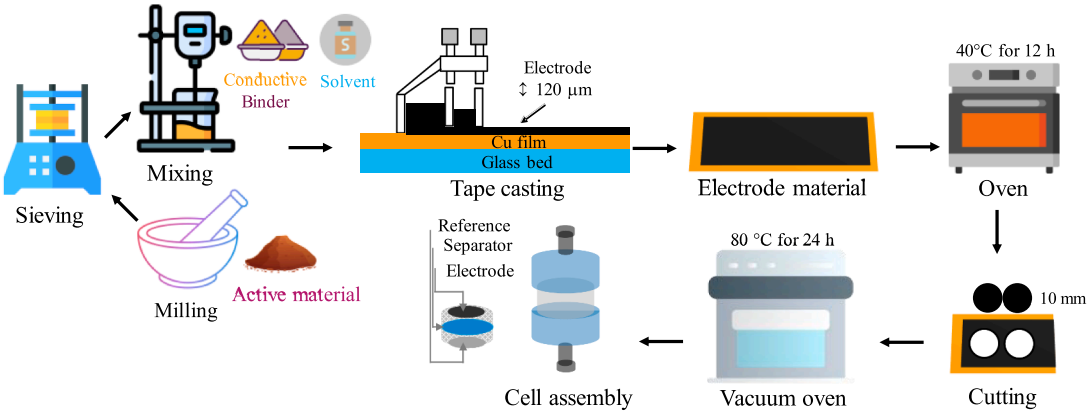

Fig. 2. Schematic representation of the electrode preparation from SiOC or SiNPs/SiOC powder.

3. Results and discussion

Fig. 3 shows the XRD patterns of the SiOC and SiNPs/SiOC ceramic composite. The spectrum of the SiOC sample shows a main broad peak centered at ≈ 24° in the range from ≈ 21° (silica/silicon oxycarbide)[33,34] to 26.5° (graphitic carbon), suggesting the formation of a disordered SiOC and free C. The presence of C_{free} is also supported by the small and broad hump in the range 40 – 45° [35]

The XRD spectrum of the as-received SiNPs shows peaks at 2θ = 28.4°, 47.3°, 56.1°, and 76.4°, which are assigned (JCPDS file 27–1402) to the (111), (220), (311), and (331) planes of cubic Si, respectively. From the line broading an average crystallite size of 44 nm is estimated. A broad hump centered at ca 2θ = 21° evidence that the Si powders are partially oxidized into silica. The spectrum of the SiNPs/SiOC composite confirms the successful incorporation of Si nanocrystals into the SiOC matrix.

FTIR spectra for both SiOC and SiNPs/SiOC powders are presented in Fig. 4. For comparison, the spectrum of the preceramic polymer, Durazane, is also included.

Almost all Si-N and Si-NH bonds present in the pre-ceramic precursor disappear during the pyrolysis and are largely replaced by Si-O bonds as shown by the FTIR spectra in Fig. 4. The spectra of the pyrolyzed samples show characteristic bands corresponding to Si-O-Si asymmetric stretching at ≈ 1070 cm^{-1} with a shoulder at 1200 cm^{-1}, Si-C stretching at 800 cm^{-1}, δ(Si-O) at 460 cm^{-1} and $C = C$ vibrations centered at 1580 cm^{-1}, which are typical features of polymer-derived inorganic SiOC ceramics [36] The formation of Si-O bonds is largely attributed to reactions with gaseous by-products (CO and CO_2),[37,38] released from PU decomposition during pyrolysis.

Fig. 5 shows the thermal oxidation behavior of the SiOC and SiNPs/SiOC samples in air up to 1450 °C, with an isothermal hold at the maximum temperature for 2 h.

Below 200 °C, both samples exhibit a minor weight loss, (≈ 3.0 wt %) due to evaporation of residual solvent and moisture, followed by a substantial mass loss between roughly 400–800 °C. This mass loss is primarily attributed to the oxidation of the excess (free) carbon phase of the SiOC matrix, according to the reaction:

$$C_{free} + O_2 \rightarrow CO_2 \quad (1)$$

This weight loss can be used to estimate the fraction of free carbon present in the pyrolyzed ceramic materials. It should be noted, however, that this represents only a rough estimate, as an exact value can be obtained only if the following conditions are met: (i) complete oxidation of the free carbon phase (i.e., 100 % oxidation), and (ii) no oxidation of carbon incorporated within the silicon oxycarbide network. With this caveat, the minimum amount of free carbon in the two samples is estimated to be 39.2 wt % for SiOC and 24.4 wt % for SiNPs/SiOC.

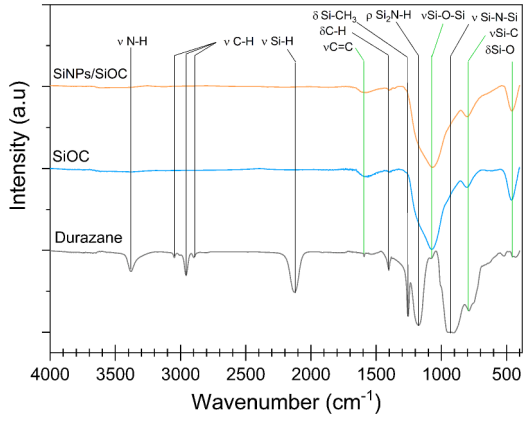

Fig. 4. FTIR spectra of the: preceramic polysilazane (Durazane); Ceramic SiOC and SiNPs/SiOC composite pyrolyzed at 900 °C.

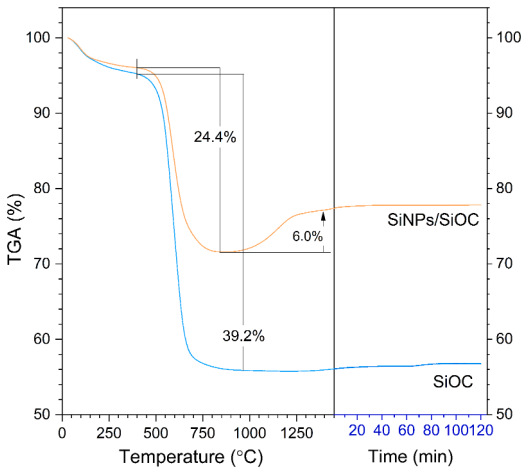

Fig. 5. TGA analysis of SiOC and SiNPs/SiOC composite samples in air at a heating rate of 10 °C min^{-1} up to 1450 °C, with an isothermal hold for 2 h at the maximum temperature.

Above 800 °C, the SiNPs/SiOC composite sample exhibits a weight gain of about 6.0 wt %, which is attributed to the oxidation of Si nanoparticles according to the reaction:

$$Si + O_2 \rightarrow SiO_2 \quad (2)$$

For this reaction, the theoretical weight increase is 113.9 %, which suggests a minimum Si content in the SiNPs/SiOC composite of 5.3 wt %.

However, based on the amount of as-received SiNPs which we added to the starting TPU (≈15 wt %) and considering the amount of impregnated Durazane as well as the weight loss during pyrolysis, we estimate the SiNPs content in the SiOC matrix to be approximately 15 wt % (details of the calculation procedure are provided elsewhere [29] It should be noted that, as revealed by the XRD analysis (Fig. 3), the starting SiNPs are partially oxidized; therefore, the estimated 15 wt % should be regarded as a maximum value. Indeed, a TGA experiment performed in air on the starting SiNPs (**Fig. SI 2**) showed, in the temperature range 800 – 1200 °C, a weight increase of 53.5 wt %, suggesting that the actual nano-Si content in the as-received SiNPs is approximately only 46.9 wt %. Accordingly, the SiNP content in the final composite can be estimated as: $\frac{46.9}{100}15 = 7.0$ *wt.*% in reasonable agreement with the value (5.3 wt %) estimated from TGA analysis. In conclusion, the actual amount of SiNPs in the SiOC matrix should be comprised in the range 5.3 – 7.0 wt %.

The skeletal density of the SiOC ceramics and the SiNPs/SiOC composite is reported in Table 1. The skeletal density of the SiNPs/SiOC composite is similar to that of the SiOC sample.

Fig. 6 presents the N_2 adsorption–desorption isotherms and corresponding pore size distributions of both samples. The isotherms exhibit a Type II behavior, which is characteristic of non-porous or macroporous systems. The neat SiOC shows a BET specific surface area of 31.9 $m^2\ g^{-1}$, whereas the SiNP/SiOC composite exhibits a slightly lower value of 26.4 $m^2\ g^{-1}$. Importantly, the total pore volume of the composite is approximately four times higher than that of neat SiOC, indicating that the incorporation of Si nanoparticles induces the formation of a certain amount of macropores. Moreover, this moderate hierarchical porosity is highly beneficial for lithium storage, as it enhances electrolyte infiltration, facilitates Li-ion transport by reducing diffusion pathways, and

Table 1
Skeletal density of SiOC and SiNPs/SiOC composite.

ρ_s	g cm^{-3}
SiOC	2.19 ± 0.05
SiNPs/SiOC	2.16 ± 0.04

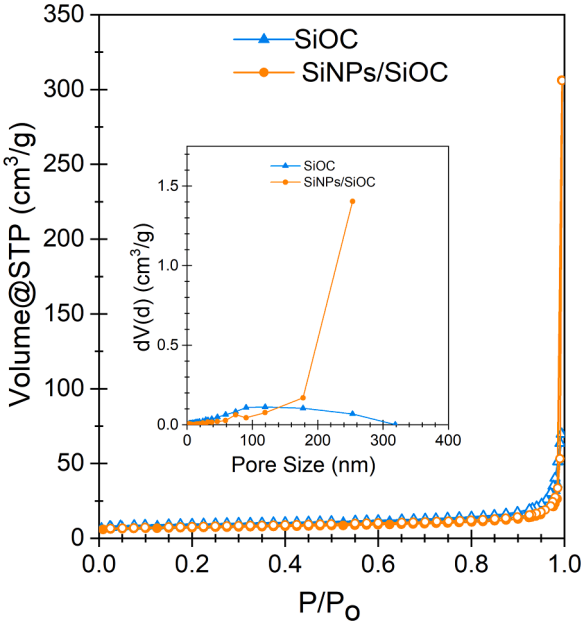

Fig. 6. Nitrogen physisorption isotherms of the SiOC and SiNPs/SiOC samples. The inset presents the pore size distribution of both materials, calculated using the BJH model. The SiOC shows a total pore volume of 0.10 $cm^3\ g^{-1}$, whereas the SiNPs/SiOC exhibits a relatively higher pore volume of 0.46 $\mathbf{cm^3\ g^{-1}}$.

provides sufficient void space to accommodate the volume change of Si during lithiation/delithiation.

Fig. 7 presents the SEM image and EDS analysis of the SiNP/SiOC composite. The SEM image, combined with EDS elemental mapping, indicates a uniform distribution of silicon nanoparticles within the SiOC network, with no evidence of significant agglomeration (see Fig. 7a and SI 3). The bright Si spots in the Si map align with high-contrast regions in the SEM image, whereas the C and O maps show an almost uniform background with only slight intensity dips at the Si sites. Additionally, the EDS maps validate the colocalization of silicon, carbon, and oxygen elements, which aligns with the formation of a SiNP/SiOC composite.

Galvanostatic cycling with potential limitation (GCPL) was conducted at various current densities to assess the specific capacity, stability, and rate capability of the electrodes. Fig. 8 illustrates the initial charge-discharge capacities of both samples measured at 74 mA g^{-1} (0.2C). The reversible capacities for the first cycle were notably high: 675 mAh g^{-1} for SiOC ceramic and 742 mAh g^{-1} for SiNPs/SiOC composite. The charge–discharge profiles of the studied materials are consistent with those reported in the literature for silicon oxycarbide [8,

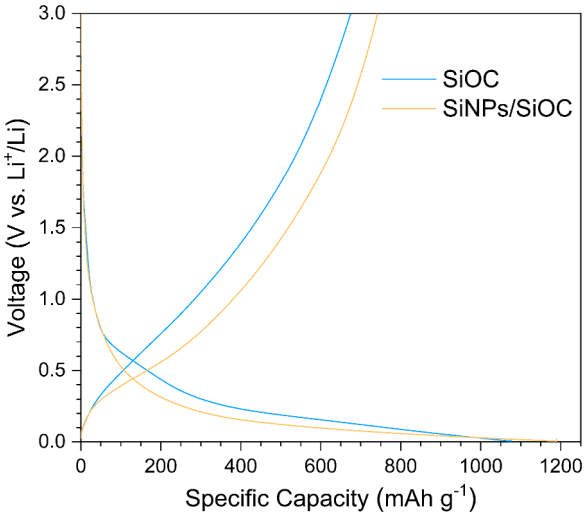

Fig. 8. First-cycle galvanostatic charge–discharge profiles of the SiOC ceramic and SiNPs/SiOC composite at a current density of 74 mA g^{-1} (C/5).

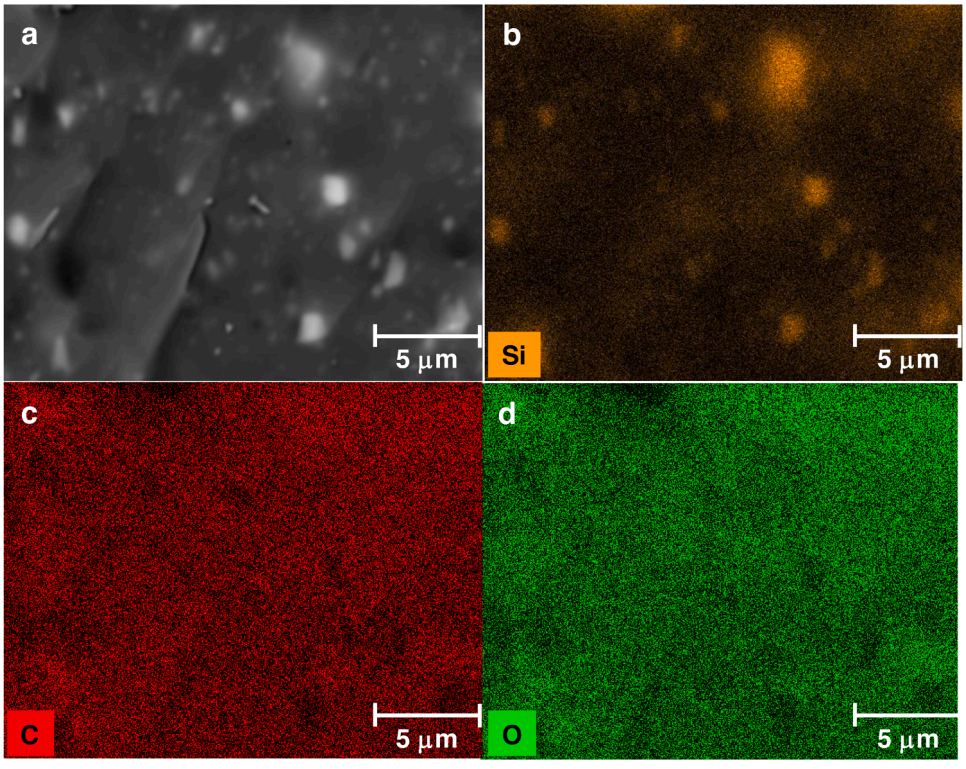

Fig. 7. SEM image and EDS analysis of SiNP/SiOC composite (a), and EDS mapping of (b) silicon, (c) carbon, and (d) oxygen elements.

39], as well as for other Si/SiOC composites [22,40,41] However, direct comparison is not always straightforward, since in some studies the amount of added Si is not reported[40], while in others, the declared Si content in the SiOC matrix is significantly higher than in our materials, thereby preventing a direct comparison. For example, Wu et al. synthesized Si/SiOC nanocomposites containing 8.7–27.8 wt % Si nanoparticles, with the sample containing 22.2 wt % Si exhibiting the best cyclic performance, delivering a reversible capacity of approximately 800 mAh g^{-1} after 100 cycles at 100 mA g^{-1} current density [22] In any case, by comparing the synthesis processes, we can conclude that the approach presented in this work is significantly simpler, straightforward, and cost-effective, which facilitates its implementation at a large scale compared to more complex methods reported in the literature for the fabrication of Si/SiOC composite materials.

Fig. 9 presents the first GCPL charging-discharging profiles recorded at 19 (C/20), 37 (C/10), and 74 (C/5) mA g^{-1} current density. The SiNPs/SiOC electrode exhibited very high first-charging capacities of 1630, 1257, and 1190 mAh g^{-1}, with corresponding discharge capacities of 990, 896, and 742 mAh g^{-1} at C/20, C/10, and C/5 ratings, respectively.

Fig. 10a displays the specific capacities and coulombic efficiencies of the SiOC and SiNPs/SiOC composite electrodes at a current density of 74 mA g^{-1}. The SiOC ceramic has an initial reversible capacity of 675 mAh g^{-1}, with 69 % capacity retention after 36 cycles. In contrast, the SiNPs/SiOC composite, which contains approximately 5.3 wt % nanosized Si nanoparticles, exhibited improved initial reversible capacity and cycling stability, reaching 742 mAh g^{-1} with 87 % retention after 36 cycles, respectively. Notably, all samples show an initial coulombic efficiency (ICE) of slightly above 60 % (see Table 2).

Table 2 summarizes the charge-discharge capacities and initial coulombic efficiencies of the SiOC and SiNPs/SiOC electrodes at various applied current densities. No significant difference in terms of ICE was observed between the electrodes. At C/10 and C/5 C-rating, both samples exhibited an ICE of approximately 63 %. However, when the current density increased to 1C, the ICE decreased slightly to approximately 50 %. Overall, the reversible capacity of the SiNPs/SiOC composite electrode increased by 38 % (after 36 cycles) and 93 % (after 100 cycles, see Fig. 10b) relative to the pure SiOC ceramic when measured at C/5 and 1C, respectively.

The GCPL tests were then extended to a higher current density of 372 mA g^{-1} to evaluate long-term stability and reversible capacity (Fig. 10b). For the SiOC ceramic, reversible capacities decreased notably over the first 5 cycles, from 342 mAh g^{-1} to 307 mAh g^{-1}, to stabilize at approximately 280 mAh g^{-1} after 20 cycles. SiNPs/SiOC composite exhibited markedly different charge-discharge behavior: its discharge capacity increased from 290 mAh g^{-1} to 530 mAh g^{-1} over 36 cycles and stabilized at around 550 mAh g^{-1} by 50 cycles, with no further capacity fading. A similar behavior has been reported for other Si/SiOC composite materials,[22,42] and it likely arises from initially hindered lithium diffusion through the active materials. Of course, this phenomenon is typically observed when the electrochemical performance is measured at higher current density. In dense or large-particle structures, limited lithium diffusion and poor electrolyte infiltration initially restrict full lithiation. Upon repeated cycling, the volumetric expansion of Si induces particle cracking and pulverization, which shortens lithium-ion diffusion paths, increases accessible active material, and improves electrolyte penetration. This mechanical refinement enhances reaction kinetics and progressive capacity release until a stable, fully activated state is achieved.

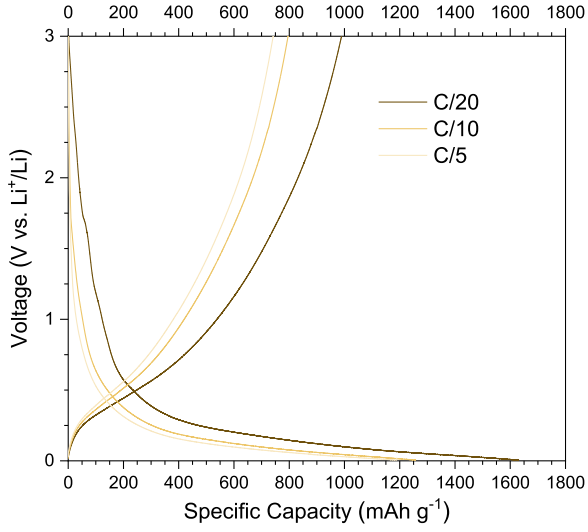

Fig. 9. First cycle galvanostatic charge–discharge curves of the SiNPs/SiOC composite recorded at different current densities.

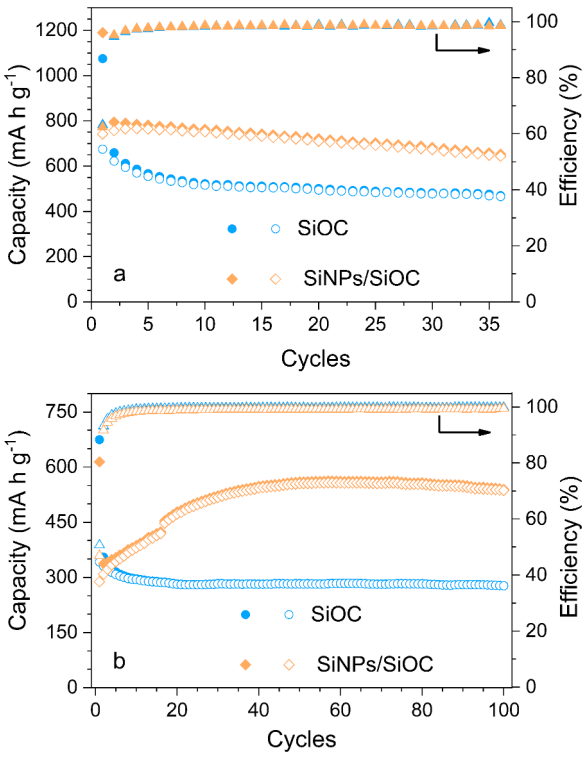

Fig. 10. Specific capacity of the SiOC ceramic and SiNPs/SiOC composite as a function of cycle number at current densities of (a) 74 mA g^{-1} and (b) 372 mA g^{-1}.

Table 2
Initial charge capacity (QC), discharge capacity (QD), and initial coulombic efficiency (ICE) of the electrodes at applied current densities of 37, 74, and 372 mA g^{-1}.

Sample	Q_C [mAh g^{-1}]			Q_D [mAh g^{-1}]			ICE [%]		
	37	74	372	37	74	372	37	74	372
SiOC	1027	1075	745	664	675	342	65	63	51
SiNPs/SiOC	1257	1190	615	796	742	288	63	62	47

Fig. 11 presents the rate performance of the SiOC ceramic and the SiNPs/SiOC composite electrode under various current densities ranging from C/10 to 3C. At a low current density (C/10), the SiNPs/SiOC composite exhibited significantly higher reversible capacities (785 mAh g^{-1}) compared to the pure SiOC sample (620 mAh g^{-1}), owing to the contribution of nanosized Si particles. As the current density increased, both electrodes showed a decrease in capacity due to increased kinetic

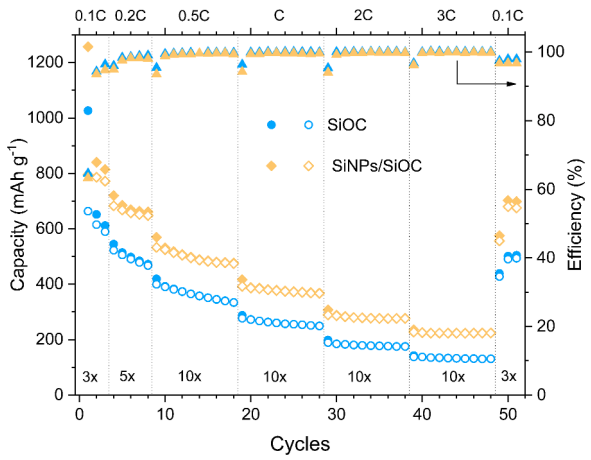

Fig. 11. Rate performance of SiOC and SiNPs/SiOC electrodes at different current densities ranging from 0.1C to 3C, followed by a return to the initial current density.

limitations. However, the SiNPs/SiOC composite maintained a much higher capacity than the SiOC ceramic. Upon returning to C/10, the SiNPs/SiOC electrode recovered 86 % of its initial capacity, indicating good structural reversibility. In contrast, the pure SiOC sample showed a relatively lower capacity recovery of approximately 72 %. The coulombic efficiencies at current densities above C/5 were approximately 99.0–100 % for both electrodes, except for the first cycle at each applied current, which was about 95 %. These results highlight the enhanced rate capability and robustness of the SiNPs/SiOC composite compared to the pure SiOC ceramic.

Fig. 12 presents the cyclic voltammetry (CV) curves of the SiOC and SiNPs/SiOC samples. The SiOC electrode showed no distinct peaks during charging and discharging. In contrast, the SiNPs/SiOC electrode exhibited a shoulder around 0.20 V during lithiation starting in the third cycle and a peak at 0.45 V during delithiation starting in the second cycle. The intensity of these peaks gradually increases with cycling, indicating progressive electrode activation, in agreement with the capacity increase reported in Fig. 8b Similar evolution of the CV curves has been reported for other Si-containing SiOC anodes [22] It appears that all the samples exhibit a similar profile during the initial cycle. However, the SiNPs/SiOC composite shows a broad cathodic shoulder at 0.20 V and another anodic peak at 0.45 V in the fifth cycle. These peaks were assigned to Li-Si alloying/dealloying.

4. Conclusion

In conclusion, a simple and efficient strategy for the fabrication of a SiNPs/SiOC composite anode for lithium-ion batteries is successfully demonstrated via the polymer-derived ceramic (PDC) route. The combination of fused filament fabrication (FFF) using a Si nanoparticle-loaded TPU filament with subsequent polymer infiltration and pyrolysis enables the production of a tailored cellular SiNPs/SiOC architecture. This approach offers a straightforward and versatile pathway for the design of structured SiNPs/SiOC composite electrodes, with potential advantages in terms of process simplicity and scalability compared to more complex routes reported in the literature.

The SiOC and SiNPs/SiOC electrodes demonstrate high reversible capacities of 675 mAh g^{-1} and 742 mAh g^{-1} at a C/5 rate, respectively. However, the SiOC system exhibits a larger capacity fading, whereas the incorporation of Si nanoparticles in the SiOC matrix results in improved cyclic stability up to 36 cycles. Furthermore, SiNPs/SiOC composite delivers a capacity of 536 mAh g^{-1}, approximately double that of SiOC (277 mAh g^{-1}), measured at 1C after 100 cycles. Regarding rate performance, both electrodes were evaluated across various C-ratings after 51 cycles, with the SiNPs/SiOC retaining 86 % of its capacity compared to 72 % for the SiOC. Consequently, the SiNPs/SiOC composite exhibits enhanced capacity, along with improved cycling stability and superior rate capability compared to SiOC alone, highlighting its potential as a promising anode material for next-generation lithium-ion batteries.

Supplementary information: The online version contains supplementary material available at

CRediT authorship contribution statement

Adane Muche Abebe: Writing – review & editing, Writing – original draft, Visualization, Methodology, Investigation, Formal analysis, Conceptualization. **Rajat Chaudhary:** Methodology, Investigation, Formal analysis, Conceptualization. **Alexander Kempf:** Investigation, Formal analysis. **Sereno Sacchet:** Investigation, Formal analysis. **Luca Fambri:** Resources, Methodology. **Mattia Biesuz:** Methodology, Conceptualization. **Magdalena Graczyk-Zajac:** Writing – original draft, Resources. **Gian Domenico Sorarù:** Writing – review & editing, Supervision, Resources, Project administration, Methodology, Funding acquisition, Conceptualization.

Declaration of competing interest

The authors declare the following financial interests/personal

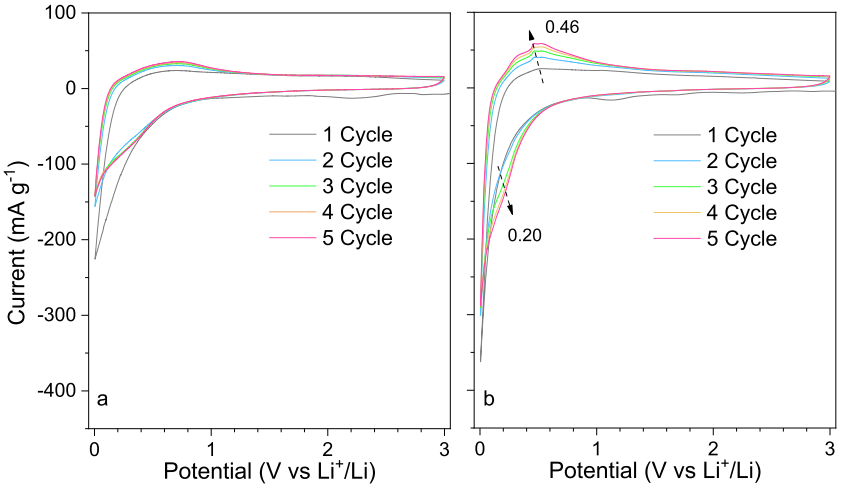

Fig. 12. Cyclic voltammograms of the first five cycles for (a) SiOC and (b) SiNPs/SiOC samples collected at a scanning rate of 50 μV/s over a potential window of 5 mV to 3.0 V.

relationships which may be considered as potential competing interests:

Adane Muche Abebe reports financial support was provided by JEST Trust. If there are other authors, they declare that they have no known competing financial interests or personal relationships that could have appeared to influence the work reported in this paper.

Acknowledgenments

Adane Muche Abebe gratefully acknowledges the financial support from JEST Trust for mobility. Rajat Chaurady and Gian Domenico Sorarù acknowledge the financial support of Fondazione Cassa di Risparmio di Trento e Rovereto (grant number 2021.0569). MGZ acknowledges the support within E-SURE. EIT Raw Materials Grant Agreement 23072.

Supplementary materials

Supplementary material associated with this article can be found, in the online version, at doi:10.1016/j.oceram.2026.100969.

References

[1] IEA, Global battery markets are growing strongly – and so are the supply risks, (2026). https://www.iea.org/commentaries/global-battery-markets-are-growing-strongly-and-so-are-the-supply-risks (accessed March 3, 2026).
[2] J. Asenbauer, T. Eisenmann, M. Kuenzel, A. Kazzazi, Z. Chen, D. Bresser, The success story of graphite as a lithium-ion anode material -fundamentals, remaining challenges, and recent developments including silicon (oxide) composites, Sustain, Energy Fuels 4 (2020) 5387–5416, https://doi.org/10.1039/d0se00175a.
[3] J. Kim, S. Jayasubramaniyan, S. Kim, D. Kim, M. Ko, N.S. Reddy, K.K. Cho, Y. G. Cho, S.Y. Nam, W. Cho, J. Sung, J. Sung, Achieving high volumetric energy density in graphite anodes through polymer coating with improved electrolyte impregnation, J. Mater. Chem. A 12 (2024) 22201–22209, https://doi.org/10.1039/d4ta03017f.
[4] P. Dibandjo, M. Graczyk-Zajac, R. Riedel, V.S. Pradeep, G.D. Soraru, Lithium insertion into dense and porous carbon-rich polymer-derived SiOC ceramics, J. Eur. Ceram. Soc. 32 (2012) 2495–2503, https://doi.org/10.1016/j.jeurceramsoc.2012.03.010.
[5] G.A. Collins, H. Geaney, K.M. Ryan, Alternative anodes for low temperature lithium-ion batteries, J. Mater. Chem. A 9 (2021) 14172–14213, https://doi.org/10.1039/d1ta00998b.
[6] M. Ashuri, Q. He, L.L. Shaw, Silicon as a potential anode material for Li-ion batteries: where size, geometry and structure matter, Nanoscale 8 (2016) 74–103, https://doi.org/10.1039/c5nr05116a.
[7] H. Ying, W.Q. Han, Metallic Sn-based anode materials: application in high-performance lithium-ion and sodium-ion batteries, Adv. Sci. 4 (2017) 1700298, https://doi.org/10.1002/advs.201700298.
[8] H. Fukui, H. Ohsuka, T. Hino, K. Kanamura, A. Si-O-C composite anode, High capability and proposed mechanism of lithium storage associated with microstructural characteristics, ACS Appl. Mater. Interfaces 2 (2010) 999–1008, https://doi.org/10.1021/am100030f.
[9] B. Santhosh, A.M. Abebe, M. Biesuz, P. Madajski, A. Zambotti, G.D. Sorarù, M. Wilamowska-Zawłocka, Electrochemical performance of polymer-derived in-situ generated nano-silicon/SiNx composite anodes for lithium-ion storage, Electroch. Acta 540 (2025), https://doi.org/10.1016/j.electacta.2025.147180.
[10] V.S. Pradeep, E. Zera, M. Graczyk-Zajac, R. Riedel, G.D. Soraru, Structural design of polymer-derived SiOC ceramic aerogels for high-rate Li ion storage applications, J. Am. Ceram. Soc. 99 (2016) 2977–2983, https://doi.org/10.1111/jace.14323.
[11] S. Bin Mujib, G. Singh, Polymer derived SiOC and SiCN ceramics for electrochemical energy storage: a perspective, Int. J. Ceramic. Eng. Sci. 4 (2022) 4–9, https://doi.org/10.1002/ces2.10108.
[12] Ying Feng, Ningning Feng, Yuzhen Wei, Yu Bai, Preparation and improved electrochemical performance of SiCN-graphene composite derived from poly (silylcarbondiimide) as Li-ion battery anode, J. Mater. Chem. A 2 (2014) 4168–4177, https://doi.org/10.1039/c3ta14441k.
[13] M. Graczyk-Zajac, D. Vrankovic, P. Waleska, C. Hess, P.V. Sasikumar, S. Lauterbach, H.J. Kleebe, G.D. Sorarù, On the Li-storage capacity of SiOC glasses with and without mixed silicon oxycarbide bonds, J. Mater. Chem. A 6 (2018) 93–103, https://doi.org/10.1039/c7ta09236a.
[14] L.M. Reinold, Y. Yamada, M. Graczyk-Zajac, H. Munakata, K. Kanamura, R. Riedel, The influence of the pyrolysis temperature on the electrochemical behavior of carbon-rich SiCN polymer-derived ceramics as anode materials in lithium-ion batteries, J. Power Sources 282 (2015) 409–415, https://doi.org/10.1016/j.jpowsour.2015.02.074.
[15] V.S. Pradeep, D.G. Ayana, M. Graczyk-Zajac, G.D. Soraru, R. Riedel, High rate capability of SiOC ceramic aerogels with tailored porosity as anode materials for Li-ion batteries, Electrochim. Acta 157 (2015) 41–45, https://doi.org/10.1016/j.electacta.2015.01.088.
[16] L.M. Reinold, M. Graczyk-Zajac, Y. Gao, G. Mera, R. Riedel, Carbon-rich SiCN ceramics as high capacity/high stability anode material for lithium-ion batteries, J. Power Sources 236 (2013) 224–229, https://doi.org/10.1016/j.jpowsour.2013.02.046.
[17] M. Wilamowska, M. Graczyk-Zajac, R. Riedel, Composite materials based on polymer-derived SiCN ceramic and disordered hard carbons as anodes for lithium-ion batteries, J. Power Sources 244 (2013) 80–86, https://doi.org/10.1016/j.jpowsour.2013.03.137.
[18] J. Kaspar, M. Graczyk-Zajac, R. Riedel, Carbon-rich SiOC anodes for lithium-ion batteries: part II. Role of thermal cross-linking, Solid State Ion. 225 (2012) 527–531, https://doi.org/10.1016/j.ssi.2012.01.026.
[19] V.S. Pradeep, M. Graczyk-Zajac, R. Riedel, G.D. Soraru, New insights in to the lithium storage mechanism in polymer derived SiOC anode materials, Electrochim. Acta 119 (2014) 78–85, https://doi.org/10.1016/j.electacta.2013.12.037.
[20] P.E. Sanchez-Jimenez, R. Raj, Lithium insertion in polymer-derived silicon oxycarbide ceramics, J. Am. Ceram. Soc. 93 (2010) 1127–1135, https://doi.org/10.1111/j.1551-2916.2009.03539.x.
[21] H. Hu, T. Cai, Y. Tong, J. Wang, L. Zhou, J. Cao, P. Liu, X. Li, A. Li, Z. Yan, W. Xing, Stepwise construction of Si–O–C and Si–C collaborative interfaces for highly stable silicon anodes, Energy Storage Mater 84 (2026) 104818, https://doi.org/10.1016/j.ensm.2025.104818.
[22] Z. Wu, W. Lv, X. Cheng, J. Gao, Z. Qian, D. Tian, J. Li, W. He, C. Yang, A nanostructured Si/SiOC composite anode with volume-change-buffering microstructure for lithium-ion batteries, Chem. Eur. J. 25 (2019) 2604–2609, https://doi.org/10.1002/chem.201805255.
[23] K. Wissel, D. Vrankovic, G. Trykowski, M. Graczyk-Zajac, Synthesis of 3D silicon with tailored nanostructure: influence of morphology on the electrochemical properties, Solid State Ion. 302 (2017) 180–185, https://doi.org/10.1016/j.ssi.2016.12.008.
[24] D. Vrankovic, K. Wissel, M. Graczyk-Zajac, R. Riedel, Novel 3D Si/C/SiOC nanocomposites: toward electrochemically stable lithium storage in silicon, Solid State Ion. 302 (2017) 66–71, https://doi.org/10.1016/j.ssi.2016.11.009.
[25] D. Vrankovic, M. Graczyk-Zajac, C. Kalcher, J. Rohrer, M. Becker, C. Stabler, G. Trykowski, K. Albe, R. Riedel, Highly porous silicon embedded in a ceramic matrix: a stable high-capacity electrode for Li-ion batteries, ACS Nano 11 (2017) 11409–11416, https://doi.org/10.1021/acsnano.7b06031.
[26] J. Kaspar, M. Graczyk-Zajac, S. Lauterbach, H.J. Kleebe, R. Riedel, Silicon oxycarbide/nano-silicon composite anodes for Li-ion batteries: considerable influence of nano-crystalline vs. nano-amorphous silicon embedment on the electrochemical properties, J. Power Sources 269 (2014) 164–172, https://doi.org/10.1016/j.jpowsour.2014.06.089.
[27] G.D. Sorarù, L. Kundanati, B. Santhosh, N. Pugno, Influence of free carbon on the Young's modulus and hardness of polymer-derived silicon oxycarbide glasses, J. Am. Ceram. Soc. 102 (2019) 907–913, https://doi.org/10.1111/jace.16131.
[28] A. Kulkarni, J. Pearce, Y. Yang, A. Motta, G.D. Sorarù, SiOC(N) cellular structures with dense struts by integrating fused filament fabrication 3D printing with polymer-derived ceramics, Adv. Eng. Mater. 23 (2021), https://doi.org/10.1002/adem.202100535.
[29] R. Chaudhary, J. Zyambo, S. Sacchet, L. Fambri, M. Biesuz, G.D. Sorarù, 3D Printing polymer derived SiC/SiOC(N) ceramic matrix composites from replica of SiC/polyurethane cellular structures, J. Am. Ceram. Soc. 109 (2026) e70635, https://doi.org/10.1111/jace.70635.
[30] A.A. Pavlovskii, K. Pushnitsa, A. Kosenko, P. Novikov, A.A. Popovich, 3D-Printed lithium-ion battery electrodes: a brief review of three key fabrication techniques, Materials 17 (2024) 5904, https://doi.org/10.3390/ma17235904.
[31] J. Wang, Q. Sun, X. Gao, C. Wang, W. Li, F.B. Holness, M. Zheng, R. Li, A.D. Price, X. Sun, T.K. Sham, X. Sun, Toward high areal energy and power density electrode for Li-ion batteries via optimized 3D printing approach, ACS Appl. Mater. Interfaces 10 (2018) 39794–39801, https://doi.org/10.1021/acsami.8b14797.
[32] R. Chaudhary, F. Agostinacchio, R. Canteri, M. Biesuz, A. Motta, G.D. Sorarù, Fabrication and characterization of SiOC(N) cellular structures via 3D-printed polyurethane templates impregnated with polysilazane, J. Eur. Ceram. Soc. 45 (2025) 117706, https://doi.org/10.1016/j.jeurceramsoc.2025.117706.
[33] G.M. Renlund, S. Prochazka, R.H. Doremus, Silicon oxycarbide glasses: part II. Structure and properties, J. Mater. Res. 6 (1991) 2723–2734, https://doi.org/10.1021/cm071203q.
[34] R. Peña-Alonso, G. Mariotto, C. Gervais, F. Babonneau, G.D. Soraru, New insights on the high-temperature nanostructure evolution of SiOC and B-doped SiBOC polymer-derived glasses, Chem. Mater 19 (2007) 5694–5705, https://doi.org/10.1021/cm071203q.
[35] F. Destyorini, Y. Irmawati, A. Hardiansyah, H. Widodo, I.N.D. Yahya, N. Indayaningsih, R. Yudianti, Y.I. Hsu, H. Uyama, Formation of nanostructured graphitic carbon from coconut waste via low-temperature catalytic graphitisation, Eng. Sci. Technol. Int. J. 24 (2021) 514–523, https://doi.org/10.1016/j.jestch.2020.06.011.
[36] M. Narisawa, F. Funabiki, A. Iwase, F. Wakai, H. Hosono, Effects of atmospheric composition on the molecular structure of synthesized silicon oxycarbides, J. Am. Ceram. Soc. 98 (2015) 3373–3380, https://doi.org/10.1111/jace.13756.
[37] R.P. Lattimer, R.C. Williams, Low-temperature pyrolysis products from a polyether-based urethane, J. Anan. Appl. Pyrolysis 63 (2002) 85–104, https://doi.org/10.1016/S0165-2370(01)00143-7.
[38] M. Wang, Z. Zhang, M.B. Ahmad, Z. Hu, N. Deng, M. Su, X. Wang, The TGA-FTIR-GC/MS characterizations of pyrolysis of polyurethane paint slags, Therm. Sci. 28 (2024) 4421–4434, https://doi.org/10.2298/TSCI2405421W.
[39] D. Knozowski, M. Graczyk-Zając, D. Vrankovic, G. Trykowski, M. Sawczak, D.M. De Carolis, M. Wilamowska-Zawłocka, New insights on lithium storage in silicon oxycarbide/carbon composites: impact of microstructure on electrochemical

properties, Compos. B Eng. 225 (2021) 109302, https://doi.org/10.1016/j.compositesb.2021.109302.
[40] B. chen Huang, L. yan Tsui, S. Ramki, H. ping Hsu, C. wen Lan, Synthesizing Si/SiOC composites through different sol-gel reaction routes for lithium-ion battery anode materials, Heliyon 10 (2024) e33612, https://doi.org/10.1016/j.heliyon.2024.e33612.
[41] Q. Li, D. Chen, K. Li, J. Wang, J. Zhao, Electrostatic self-assembly bmSi@C/rGO composite as anode material for lithium ion battery, Electrochim. Acta 202 (2016) 140–146, https://doi.org/10.1016/j.electacta.2016.04.019.
[42] P. Lv, H. Zhao, C. Gao, Z. Du, J. Wang, X. Liu, SiOx-C dual-phase glass for lithium ion battery anode with high capacity and stable cycling performance, J. Power Sources 274 (2015) 542–550, https://doi.org/10.1016/j.jpowsour.2014.10.077.